

# Coverage-Induced Cation Dehydration and Migration for Enhanced CO–CO Coupling on Cu Electrocatalysts

Hui-Min Yan, Zisheng Zhang, and Yang-Gang Wang\*

Cite This: *ACS Catal.* 2024, 14, 3596–3605

Read Online

ACCESS |



Metrics &amp; More



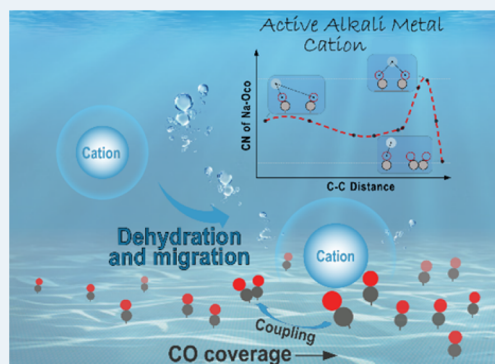
Article Recommendations



Supporting Information

**ABSTRACT:** Copper is a promising catalyst for the electroreduction of CO<sub>2</sub>/CO (CO<sub>2</sub>RR/CORR) to valuable multicarbon products, but the origin of its CO–CO coupling activity remains unresolved. This greatly limits the rational design and practical application of copper-based catalysts. Herein, we have performed extensive ab initio molecular dynamics simulations with explicit solvation to investigate the free energy profile of CO–CO coupling at the complex electrochemical interface and discovered the critical role of the interplay between the alkali metal cation and CO intermediates. We have found that due to the hydrophobicity of CO, the solvated alkali metal cation (Li<sup>+</sup>, Na<sup>+</sup>, K<sup>+</sup>, or Cs<sup>+</sup>) in the electric double layer (EDL) could dynamically dehydrate and migrate toward the copper surface as the CO coverage increases. The closer-to-surface dehydrated alkali metal cation can significantly promote CO–CO coupling by stabilizing the largely polarized transition state. Notably, once CO–CO coupling is completed, the cation can be released from the product state to participate in the next catalytic cycle. The adaptive coordination environment of the alkali metal cation to the reaction coordinate makes a dynamic local environment which promotes CO–CO coupling both kinetically and thermodynamically. Our obtained insight into the dynamic process unravels the significant role of alkali metal cations and provides a perspective to understand how C<sub>2</sub> products are generated at the complex electrochemical interface during the CO<sub>2</sub>RR/CORR.

**KEYWORDS:** CO<sub>2</sub> reduction reaction, CO–CO coupling, cation effect, coverage effect, explicit solvation



## 1. INTRODUCTION

The electrochemical reduction of CO<sub>2</sub> (CO<sub>2</sub>RR) into high-value hydrocarbon products is a promising solution for renewable energy storage and CO<sub>2</sub> recycling.<sup>1–5</sup> Among the known transition metals, the copper-based catalyst<sup>2,6</sup> is of great fundamental and practical interest for it could give multicarbon items, with ethylene and ethanol as the major C<sub>2</sub> products.<sup>7–9</sup> Although extensive studies have been devoted to exploring the key factors, such as the electrolyte cations,<sup>10–14</sup> CO coverage,<sup>15–19</sup> and pH,<sup>20–22</sup> that may determine the conversion of the CO<sub>2</sub>RR toward the C<sub>2</sub> product, it remains a grand challenge to fully understand the C–C coupling process due to the complexed electrochemical interface.

At present, there is still much speculation about the intermediates that can participate in C–C coupling. In this regard, several C<sub>1</sub> species (such as \*CO, \*CHO, and \*COH) have been proposed to enter the C–C coupling process.<sup>22–25</sup> Specifically, under relatively moderate potentials ( $U$  at  $-0.6 \sim -0.8$  V vs  $U_{\text{RHE}}$ ), the C–C coupling between \*CO species is broadly demonstrated as a dominant pathway to C<sub>2</sub> products,<sup>24–26</sup> which is also suggested as the rate-determining step (RDS) separating from C<sub>1</sub> productions due to the pH-independent ethylene production.<sup>20,26,27</sup> Importantly, ethylene production is closely related to the CO coverage. Huang's

work has evidenced that ethylene was formed only after the in situ generated \*CO reaches a significant concentration threshold.<sup>18</sup> In contrast, recent work by Xu's group suggests the hydrogenation of CO with adsorbed water is the RDS for multicarbon products on the Cu electrode,<sup>28</sup> deduced from the CO reaction order being or below unity. Nonetheless, the carbon source of multicarbon products eventually comes from the CO species; C–C coupling is the inevitable step to yield C<sub>2</sub>+ products no matter which type of coupling pathway is dominant. CO–CO coupling, serving as a primary model reaction, is of great significance for understanding the complicated C–C coupling mechanism.

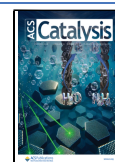
It is well known that the alkali metal cations in the electrolyte greatly promote the rate of C–C coupling with the increasing ionic radius (Li<sup>+</sup> < Na<sup>+</sup> < K<sup>+</sup> < Cs<sup>+</sup>),<sup>10,12,29,30</sup> but the origin of the cation-enhanced selectivity for the C<sub>2</sub> product remains unclear. Resasco and Chen et al. proposed that alkali

Received: November 29, 2023

Revised: February 6, 2024

Accepted: February 7, 2024

Published: February 20, 2024



metal cations present an interfacial electric field varying with its effective hydration radius, which greatly stabilizes the more polarized \*CO<sub>2</sub> and \*OCCO intermediates due to the strong dipole-field interaction and leads to an enhanced C<sub>2</sub> production.<sup>13,29</sup> However, the interplay between alkali metal cations and the key intermediates is not limited to the nonbonded electrified field effect.<sup>11,31,32</sup> AM cations may also directly coordinate to the adsorbed species and form a cation-adsorbent complex, as demonstrated by Koper and group<sup>33</sup> and Hansen and group.<sup>34</sup> Specifically, recent works by Chen and group and Choi and group have identified cation-coordinated \*OCCO intermediates by AIMD simulations and suggested that larger cations can more easily bind two adjacent \*CO reactants, resulting in facile C–C bond formation than smaller cations.<sup>35</sup> However, Kim and Choi et al. claimed that the promoted CO<sub>2</sub>RR originates from the enhanced electron transfer due to the direct binding of cations to reaction intermediates.<sup>36</sup> Despite this, how cations in the fully hydrated form dynamically participate in C–C coupling is still unclear, considering that the interplay between AM cations and adsorbates may be closely related to the hydration layer of AM cations. In a word, there is still no unified conclusion about the C–C coupling mechanism. This can be attributed to the complexity of the electrochemical interface, which is extremely challenging to study from both experimental and theoretical perspectives. The lack of comprehensive understanding of CO–CO coupling related to CO coverage, electrolyte cations, and solvent environment at an atomic level hampers rationalizing the experimental activity and selectivity for C<sub>2</sub> products on the Cu electrode, which underlies the optimization of Cu-based CO<sub>2</sub>RR electrocatalysts.

Herein, we employed ab initio molecular dynamics simulations with the explicit inclusion of the key interfacial components: surface adsorbates, alkali metal cations, and the solvent water to investigate CO–CO coupling in a dynamic view. We have identified \*CO coverage-dependent dehydration and migration dynamics of cations at the Helmholtz layer. Under low CO coverage, the cation (Na<sup>+</sup> as an example) stays hydrated and outside the contact layer, stabilized over the Cu electrode surface by electrostatics. At increasing CO coverage, the cation migrates toward the Cu electrode and partially dehydrates, interacting with the \*CO adsorbates to form a complex intermediate. The cation in this complex intermediate can modulate the free energetics of CO–CO coupling in a dynamic quasi-adsorption state. This work provides a detailed atomistic insight into the dynamic coordination environment of alkali metal cations as it interacts with surface \*CO adsorbates and how such dynamics governs the CO–CO coupling reactivity on Cu surfaces.

## 2. COMPUTATIONAL METHODS

All Born–Oppenheimer molecular dynamics (BOMD) simulations and constrained MD simulations were performed using the Vienna ab initio simulation package (VASP).<sup>37,38</sup> The core–valence electron interactions were represented by the projector augmented wave (PAW) method.<sup>39</sup> The electron exchange–correlation energies were calculated using the generalized gradient approximation (GGA)<sup>40</sup> with the Perdew–Burke–Ernzerhof (PBE) functional.<sup>41</sup> The Kohn–Sham valence states were expanded in a plane-wave basis set with a cutoff energy of 400 eV.<sup>37</sup> The Cu(3d, 4s), O(2s, 2p), H(1s), C(2s, 2p), and Na(1s) electrons were treated as valence

states. The second-order Methfessel–Paxton scheme with a smearing width of 0.1 eV was set for specifying the partial occupancies. The self-consistent field (SCF) convergence criterion was set to 10<sup>−5</sup> eV for both the electronic gradients and total energies. Grimme’s D3 dispersion correction was adopted to better describe the noncovalent interactions.<sup>42</sup> A  $\gamma$  *k*-point mesh was used to sample the Brillouin zone. The MD simulations were sampled by the canonical (NVT) ensemble employing Nose–Hoover thermostats,<sup>43,44</sup> and each simulation lasted for 15–20 ps with a time step of 1.0 fs at 298 K. The atomic mass for the H atom was set to be 2.0 to get the longer time step of 1 fs in AIMD runs.

To benchmark the validation of PBE-D3, we also calculated the potential energy curves of CO coupling by RPBE and BEEF\_VDW functionals, which showed that PBE-D3 can properly reproduce the potential energy surface for CO coupling, as done by RPBE and BEEF\_VDW. And the test details are given in Figure S1 of the Supporting Information (SI). In this work, we focus more on the hydration dynamics of the cations and the interfacial water organization, and PBE has been tested by us to perform well for these purposes.<sup>45,46</sup>

The Cu electrode was modeled by a 5 × 5 Cu(100) surface slab with four Cu layers and the bottom two layers were fixed in AIMD calculation. The box with the dimensions of 12.61 × 12.61 × 26.13 Å<sup>3</sup> was allowed to repeat periodically in all three dimensions. The procedure to construct the aqueous phase model is shown in Figure S2. The Cu electrode/water interface was modeled by filling the vacuum region with 89 water molecules, which could maintain the average water density in the bulk regions being around 1 g/cm<sup>3</sup>. The radial distribution functions (RDFs) and the coordination number (from the integration of the RDFs) of O–O and O–H for validation of the liquid water structure are also provided in Figure S4, which validates the proper convergence of the water structure to bulk behaviors. Based on the clean Cu electrode/water interface model, different numbers of CO (*n* = 1, 3, 6, 12) were inserted into the interfacial region to build a series of CO-covered Cu(100)/water models, where the number of water molecules is 89, 88, 86, and 81, respectively. The details of the model setup of different electrocatalytic interfaces used in this work are given in the SI (Figures S2–S9).

In order to evaluate the reaction free energetics of the CO coupling step, the free energy profiles are obtained by the thermodynamic integration (TI) method, where the reaction free energy and kinetic barrier are obtained by applying a holonomic constraint on the reaction coordinate ( $\zeta$ ) during MD simulations and integrating over the average unbiased force associated with the reaction coordinate,<sup>42,47</sup> as shown in the following equation

$$\Delta A(\zeta_a, \zeta_b) = - \int_{\zeta_b}^{\zeta_a} F(\zeta) d\zeta$$

where  $\Delta A(\zeta_a, \zeta_b)$  is the free energy difference between two reaction coordinates ( $\zeta_a$  and  $\zeta_b$ ) and  $F(\zeta)$  is the averaged constrained force. For the CO–CO coupling of two \*CO, the distance between two target C atoms is chosen as the collective variable (CV), which is the characteristic variable between the initial state (2\*CO) and the final state (\*OCCO) and is defined as  $CV = \zeta(r) = |r_{C1} - r_{C2}|$ , where  $r_{C1}$  and  $r_{C2}$  refer to the coordinates of the C atoms of two target \*CO, respectively. We have sampled 16 windows at  $\theta_{CO} = 3/25$  ML and 13 at  $\theta_{CO} = 6/25$  ML, with and without Na<sup>+</sup>. For all of

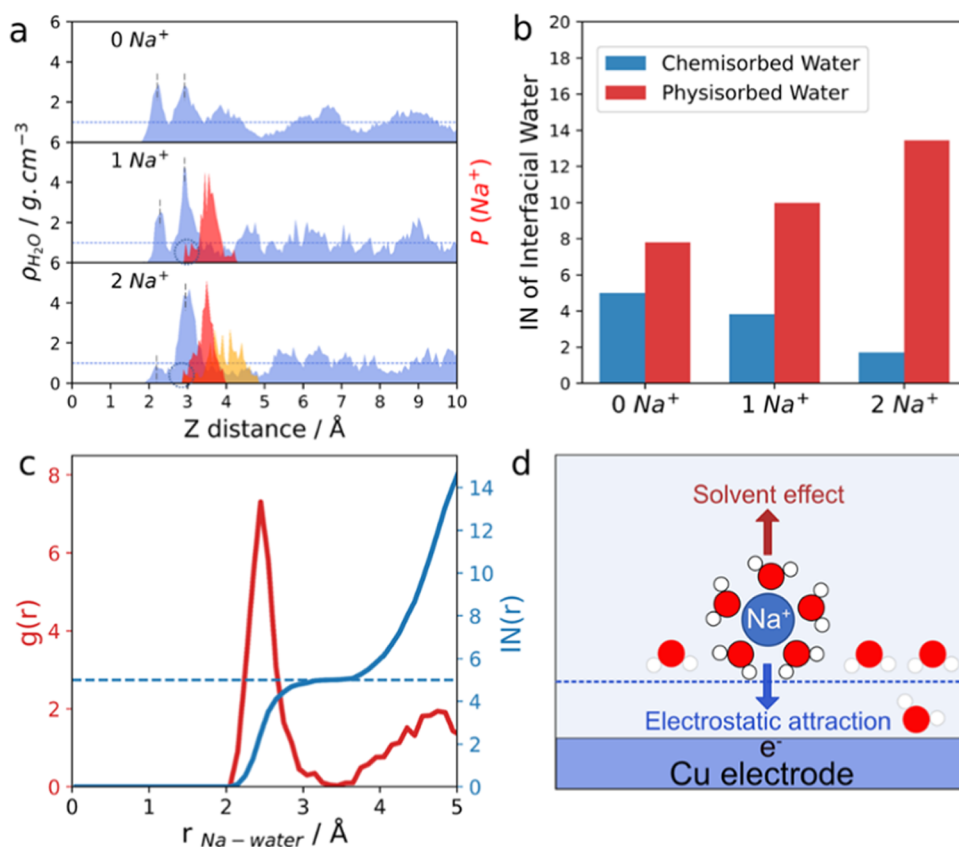


**Figure 1.** (a) Water density distribution ( $\rho_{\text{H}_2\text{O}}$ ) and the density distribution of  $\text{Na}^+$  ( $P(\text{Na}^+)$ ) along the surface normal with different number of counterions. The distributions for the 1st and 2nd  $\text{Na}^+$  ions are colored in red and yellow, respectively. (b) Number of interfacial water molecules by integrating the  $\rho_{\text{H}_2\text{O}}$ . (c) Radial distribution function of O in water around Na cations,  $g(r)$  (red line) and the corresponding integration of  $g(r)$ ,  $IN(r)$  (blue line). (d) Schematics of the counterions at the interfacial region.

the cases, we first performed 2 ps constrained MD for sampling each image. We noted that the system with the added cation takes longer to equilibrate due to the longer relaxation time of the hydration shell than that of pure water. Therefore, in the case with cations, the simulation time was added to 7–10 ps. The averaged force along the constraint of the last 2 ps was used for calculating the free energy surface. The three zero-force points in the PMF vs the C–C distance curves along the reaction coordinate correspond to the initial, transition, and final states (denoted as IS, TS, and FS). More details are given in the SI. The charges along the reaction pathway were tracked by averaging the charges of selected configurations from the last 2 ps MD trajectories via single-point energy calculations.

The radial distribution functions (RDFs) are calculated using the analysis model in VMD software version 1.9.4a48.<sup>48</sup> For the coordination number (CN) calculations of cations with the reactant CO molecules, the distance cutoff ( $d_{\text{cutoff}}$ ) for the  $\text{Na}^+$  ion and the O atom of the reactant \*CO is set as 3 Å, based on the RDF diagram given in Figure S10.

### 3. RESULTS AND DISCUSSION

**3.1. Solvation of Alkali Metal Cations at the Cu/Water Interface.** Alkali metal cations in the EDL are reported to play an important role in CO–CO coupling on the Cu surface.<sup>10–14</sup> We start from exploring their dynamic behaviors at the interface. First, we introduce one or two Na atoms into the equilibrated Cu/water interface and re-equilibrate the system for ~20 ps by AIMD simulations. Due to the weak electron affinity of the Na atoms, they would transfer electrons to the

copper surface and yield  $\text{Na}^+$  during the self-consistent field cycles, establishing the Helmholtz layer over the Cu surface.<sup>37,38</sup> Referred to the experimental Helmholtz capacitance, the estimated potentials corresponding to the interfacial concentration of 0  $\text{Na}^+$ , 1  $\text{Na}^+$ , and 2  $\text{Na}^+$  (per simulation box) are 0.29, –0.02, and –0.31 V vs RHE, respectively (see the SI for details). Since the capacitance under realistic conditions is difficult to be accurately determined, these values are only used for qualitative comparison. For simplicity, we only take the number of cations per simulation box, which corresponds to the interfacial cation concentration, to represent different reduction potentials in the following discussions.

To analyze the structure of interfacial water, we plotted the water density  $\rho_{\text{H}_2\text{O}}$  along the surface normal direction of the electrode with different amounts of interfacial  $\text{Na}^+$  in the bulk solvent (i.e., under different potentials), as shown in Figure 1a. For all three cases, the profiles of  $\rho_{\text{H}_2\text{O}}$  exhibit two distinct peaks with  $\rho_{\text{H}_2\text{O}}$  significantly larger than 1  $\text{g}/\text{cm}^3$ , indicating a water bilayer structure at the interfacial region. The first peak at ~2.2 Å represents chemisorbed water in a more rigid local solvation network. The second peak at ~2.9 Å represents physisorbed water. The numbers of both types of interfacial water in the presence of cations are displayed in Figure 1b. With the increased number of  $\text{Na}^+$ , less water gets concentrated in the first layer, while more water locates in the second layer. This indicates the partial dehydration of the Cu surface and an accumulation of the physisorbed water shell at a more negative electrode potential.

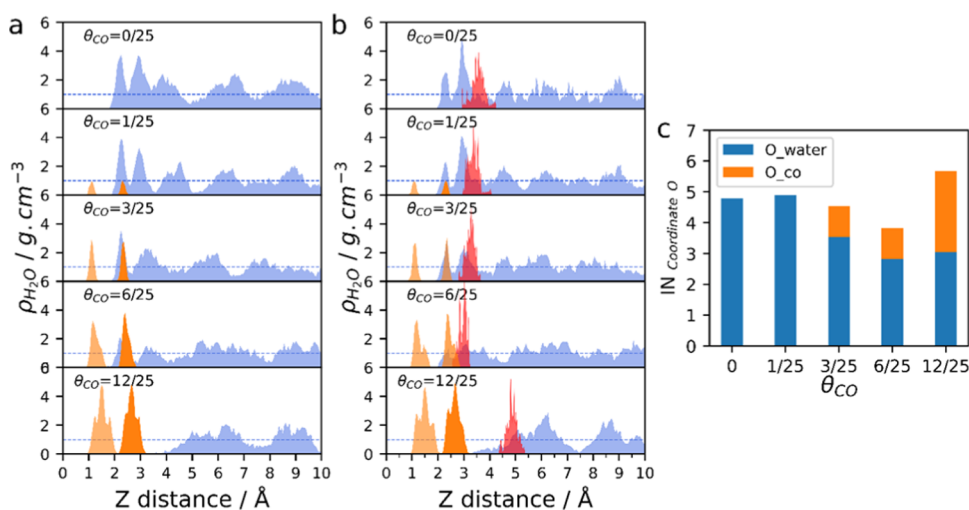


**Figure 2.** (a) Density distribution of water ( $\rho_{\text{H}_2\text{O}}$ ) and the density distribution of adsorbed CO on the Cu surface under different CO coverages. (b) Water density distribution ( $\rho_{\text{H}_2\text{O}}$ ) and the probability density of <sup>\*</sup>CO as well as Na<sup>+</sup> under different CO coverages. The light orange, orange, and red peaks represent C in <sup>\*</sup>CO and O in <sup>\*</sup>CO and Na<sup>+</sup>, respectively. The blue dashed line indicates the averaged water density in bulk water. (c) Coordination number (CN) of Na<sup>+</sup> under different CO coverages. The blue and orange bars represent the population of water and CO that are coordinated to the Na<sup>+</sup> ion, respectively.

To investigate the location of Na<sup>+</sup> at the interface, the density distributions of Na<sup>+</sup>, P(Na<sup>+</sup>), along the normal direction of the surface are also presented in Figure 1a, as seen in the red or yellow peaks. We analyzed the distribution of Na<sup>+</sup> by collecting the distances of Na<sup>+</sup> relative to the Cu surface, based on the sampled AIMD trajectories, and then obtained the time-averaged value along the normal direction. In both cases, Na<sup>+</sup> is mainly centralized in the region of 3.5–4.5 Å above the Cu electrode surface. Interestingly, the peak of Na<sup>+</sup> is always slightly behind the second peak of interfacial water, with only a few tails in the second water shell (marked by a blue circle), implying that the strong solvation effects can effectively stabilize Na<sup>+</sup> and prevent it from approaching the electrode surface. To depict the hydration shell of Na<sup>+</sup> at the Cu/water interface, we obtained the RDFs of water molecules around Na<sup>+</sup> cations, as shown in Figure 1c. The pronounced peak at 2.15–3.15 Å represents the full hydration shell of Na<sup>+</sup>, which consists of five water molecules, as estimated by the integration area of the first peak. The solvation effect of the Na<sup>+</sup> ion counteracts the electrostatic attraction posed by the negatively charged Cu electrode surface and keeps Na<sup>+</sup> from specific adsorption (as shown in Figure 1d), which differs from the situation under a particular CO coverage (*vide infra*).

**3.2. Dynamic Interplay between the Alkali Metal Cation and CO Intermediates.** Since the selectivity of the CO<sub>2</sub>RR toward multicarbon products greatly depends on CO coverage,<sup>18</sup> we further simulated the dynamics of the complex electrochemical interface in the presence of CO adsorbates. Prior to the simulations, it is necessary to ensure the possible CO coverage under realistic conditions. We have also calculated the CO adsorption free energy, as shown in Figure S11, which suggests that the CO coverage of 12/25 ML could be easily reached. The initial configurations for a series of CO-covered Cu/water systems are shown in Figure S7. We note that the recent work by Xu et al. has suggested that CO coverage on the Cu electrode at electrochemical conditions is very low (about 0.05–0.15 ML) according to the observation of surface-enhanced infrared absorption spectroscopy (SEIRAS).<sup>28</sup> However, the carbon source of multicarbon products

eventually comes from the CO species; C–C coupling is the inevitable step to yield C<sub>2</sub> products, no matter what coupling pathway (CO–CO, CO–CHO, or other C<sub>1</sub> species). This implies that CO species must be locally close to each other for the coupling process, which results in the local high coverage than the apparent low coverage. In the present work, we intend to use CO coverage as a variable parameter to investigate the coverage effect on the CO–CO coupling process. Several possible CO coverages represented by  $\theta_{\text{CO}} = 1/25, 3/25, 6/25,$  and 12/25 monolayer (ML) were simulated as suggested by the surface science characterizations performed under ultrahigh vacuum conditions.<sup>49–52</sup> Specifically, the upper limit of the CO saturation coverage on the Cu surface is suggested to be 0.25 ML under high CO pressure (60 bar),<sup>16</sup> which well supports the case of  $\theta_{\text{CO}} = 6/25$  ML that is mainly discussed in this work. The distance between two adjacent CO under  $\theta_{\text{CO}} = 6/25$  ML in this work is  $\sim 3.5$  Å, which is at a reasonable distance for CO–CO coupling. As a result, our work should be able to provide useful theoretical implications for CO coupling under realistic conditions.

We first explore the interplay between <sup>\*</sup>CO and water by analyzing the water density distribution ( $\rho_{\text{H}_2\text{O}}$ ) and the density distribution of <sup>\*</sup>CO in the CO@Cu/water systems. As shown in Figure 2a, at  $\theta_{\text{CO}} < 6/25$  ML, interfacial water maintains a bilayer structure, as evidenced by two distinct peaks in the range of 1.9–3.4 Å. Despite this, the peaks for chemisorbed and physisorbed water at the interfacial region decreased monotonically at increasing CO coverage, suggesting an enhanced repulsion between the <sup>\*</sup>CO layer and interface water. Then, it is reasonable to infer that the <sup>\*</sup>CO accumulating on the Cu electrode surface should gradually displace chemisorbed water due to its stronger binding strength than water. At  $\theta_{\text{CO}} = 12/25$  ML, a separation of ca. 1 Å is observed between the <sup>\*</sup>CO layer and the water solvent, indicating a very low water density above the <sup>\*</sup>CO layer due to the strong hydrophobicity of the saturated CO layer.

We further explore the interaction of CO species with the interfacial cations by adding Na atoms into the interfacial region. Figure 2b displays the density distributions for <sup>\*</sup>CO,

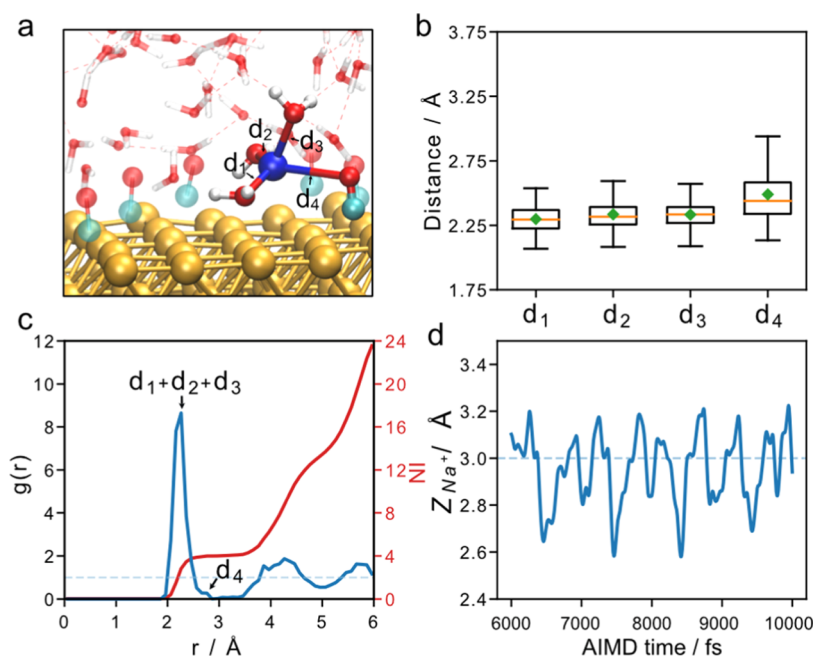


**Figure 3.** Coordination configuration of the  $\text{Na}^+$  cation at the interfacial region at  $\theta_{\text{CO}} = 6/25$  ML. (a) MD snapshots of the cation–adsorbate intermediate. The Cu, O, H, C, and Na atoms are colored yellow, red, white, cyan, and blue, respectively. (b) Distances between the  $\text{Na}^+$  ion and the adjacent water molecule or the adsorbed  $^*\text{CO}$  species. (c) Radial density function for the oxygen atoms surrounding the  $\text{Na}^+$  ion. (d) Z distance evolution between the  $\text{Na}^+$  ion and the Cu surface.

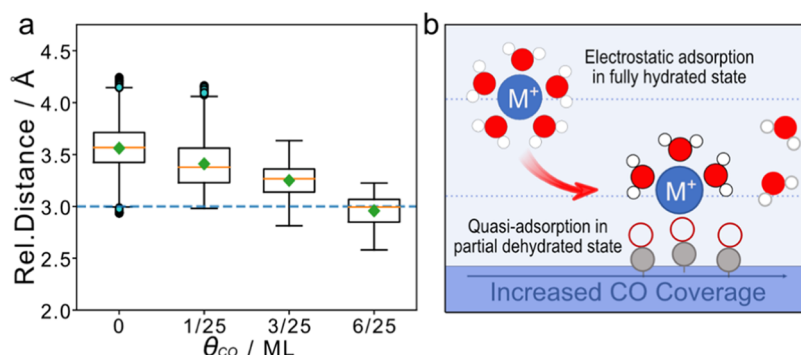


**Figure 4.** (a) Relative distance of the  $\text{Na}^+$  ion from the Cu surface under different CO coverages. (b) Schematics of the migration of cations toward the Cu surface.

water, and the  $\text{Na}^+$  ion under different CO coverages. Interestingly, with the increase of CO coverage from 0/25 to 6/25 ML, the  $\text{Na}^+$  ion gradually moves toward the Cu surface. This interesting phenomenon has also been observed in the presence of other alkali metal cation ions, such as  $\text{Li}^+$ ,  $\text{K}^+$ , and  $\text{Cs}^+$ , and the details are given in Figures S12–13. When the CO coverage is increased to 12/25 ML, the  $\text{Na}^+$  ion moves back to the water layer and gets rehydrated. The reason can be attributed to the fact that the dense  $^*\text{CO}$  layer blocks the Cu surface, which leads to  $\text{Na}^+$  supported by the  $^*\text{CO}$  layer having no access to the Cu surface. Simultaneously, the profiles of  $\rho_{\text{H}_2\text{O}}$  at the interfacial region gradually declined with the increase of CO coverage, as indicated by the decreased peaks in the range of 1.9–3.4 Å, consistent with the cases in the absence of  $\text{Na}^+$ . These findings imply that the density of interfacial water is greatly influenced by CO coverage, which further affects the solvation of the  $\text{Na}^+$  ion. We then infer that the migration dynamics of the alkali metal cation is related to the evolution of its hydration structure. To confirm this, we look into the statistics of coordination numbers (CNs) of the

$\text{Na}^+$  ion by water during the AIMD simulations (see Figure S14 for details). As shown in Figure 2c, the CNs of water around the  $\text{Na}^+$  ion decrease from 4.8 to 2.8 with CO coverage increasing from 0 to 6/25 ML, which proves that the increased CO coverage promotes the dehydration of the  $\text{Na}^+$  ion due to the increasing hydrophobicity of the  $\text{CO@Cu}(100)$  surface. This rationalizes the migration of the  $\text{Na}^+$  ion toward the Cu surface, that is, a higher CO coverage weakens the hydration of the  $\text{Na}^+$  ion, and the electrostatic attraction draws the  $\text{Na}^+$  ion migrating toward the Cu surface. Such migration is only possible after taking into account the change of the  $\text{Na}^+$  hydration structure and the interfacial water organization.

We next focus on the interplay between CO and the  $\text{Na}^+$  cation under  $\theta_{\text{CO}} = 6/25$  ML due to the CO coverage-dependent dynamics at the interfacial region. Extracting from the MD trajectory, the  $\text{Na}^+$  ion is found directly bound to one of  $^*\text{CO}$  via the O atom, as depicted in Figure 3a. To understand this intriguing adsorption state, we analyzed the coordination environment of the  $\text{Na}^+$  ion by counting the  $\text{Na}^+$ –ligand distances, as shown in Figure 3b. The distances

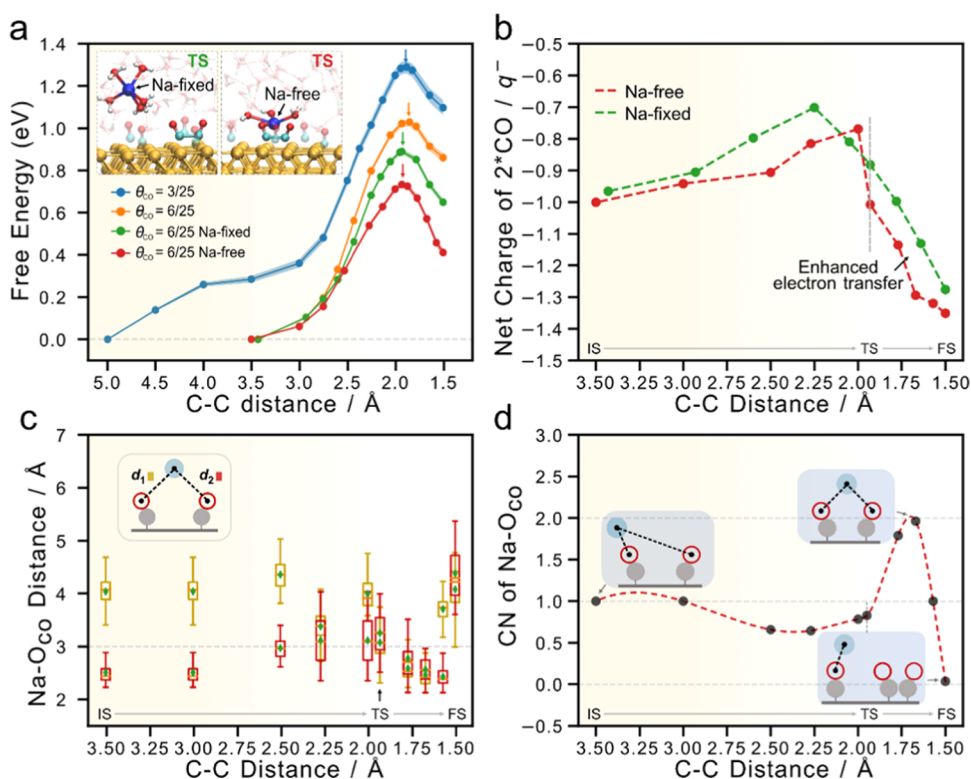


**Figure 5.** (a) Free energy profiles for CO–CO coupling to give  $^*OCCO$  intermediates. The blue, orange, green, and red lines represent the reactions at  $\theta_{CO} = 3/25$  ML,  $\theta_{CO} = 6/25$  ML,  $\theta_{CO} = 6/25$  ML with one Na atom fixed above the Cu(100) surface, and  $\theta_{CO} = 6/25$  ML with a free  $Na^+$  at the interfacial region, respectively. The transition state is indicated by an arrow. (b) Evolution of Bader charge on the reactant  $^*CO$  species during CO–CO coupling. (c) Boxplot for the Na–Oco distance. (d) Evolution of the coordination number for Na with the reactant  $^*CO$  during CO–CO coupling.

between the  $Na^+$  ion and three coordinating water molecules (labeled as  $d_{1-3}$ ) are approximately equal, while that between the  $Na^+$  ion and the  $^*CO$  species (labeled as  $d_4$ ) shows a larger value. The RDFs represented in Figure 3c show a zero-probability distribution between the pronounced peaks and the retained part, demonstrating a stable coordination environment of the  $Na^+$  ion, while Figure 3d shows the distance evolution between the  $Na^+$  ion and the Cu slab at  $\theta_{CO} = 6/25$  ML in the range of 2.6–3.2 Å, indicating that the  $Na^+$  ion should dynamically adsorb on the Cu surface.

Finally, Figure 4 presents a short summary for the interplay between CO intermediates and the cations. Figure 4a displays the distance evolution of the  $Na^+$  ion from the Cu surface. Under low CO coverage,  $Na^+$  is relatively away from the surface, where the alkali cations are well solvated by the solvent water and electrostatically interact with the Cu surface beyond the contact layer. With the increase of CO coverage, the counterions gradually migrate toward the Cu surface and partially dehydrate, as illustrated in Figure 4b. In this case,  $Na^+$  interacts with the Cu surface via a quasi-adsorption state, where the  $Na^+$  ion binds to both surface-adsorbed CO and the adjacent water molecules, forming a dynamical complex on the Cu surface.

**3.3. Enhanced CO–CO Coupling from Coverage-Induced Cation Dehydration.** Above, we have identified the CO coverage-dependent migration dynamics of interfacial alkali metal cations, which could exert an enhanced interfacial electric field on polar reaction intermediates on the surface. Herein, we investigate the effect of cation migration on CO–CO coupling for two  $^*CO$  to give  $^*OCCO$  species by

constructing the free energy profile, which is a critical elementary step in the early stage toward the formation of ethylene.<sup>49,50</sup> Given that CO–CO coupling is sensitive to other factors, we also considered the effect from CO coverage and the electrode potential. The details of the free energy sampling by thermodynamic integration are shown in the SI.

We first discuss the effect of CO coverage and the electrode potential on CO–CO coupling. As shown in Figure 5a, the free energy barriers for CO–CO coupling at  $\theta_{CO} = 3/25$  and  $6/25$  ML are 1.29 and 1.02 eV, respectively, which indicates an improved activity of  $^*CO$  coupling at a higher CO coverage. This can be attributed to the shortened average distance between two adjacent CO species (Figure S15) and the weaker binding strength of CO to the Cu surface under a higher CO coverage. For the electrode potential effect, we introduce different amounts of Na counterions in the system to modulate the surface charge and shift the workfunction, as described in Section 3.1. Compared to the case in the absence of the counterion, one  $Na^+$  counterion should lead to about a  $-0.3$  V shift for the electrode potential. To decouple the potential effect from the cationic effect, we also test the effect of the distance between  $Na^+$  and the Cu surface, which suggests a neglectable change of the surface electron density (Table S2). Under  $\theta_{CO} = 6/25$  ML, compared to the neutral case, the activation barrier with a counterion fixed at a specific distance (i.e.,  $\sim 5.9$  Å, so as to no interact with surface adsorbates) above the Cu slab exhibits a decrease by 0.13 eV, which suggests that the  $^*CO$  coupling is promoted at a more negative potential. We note that the free energy profiles here were not sampled under constant potential conditions, while based on

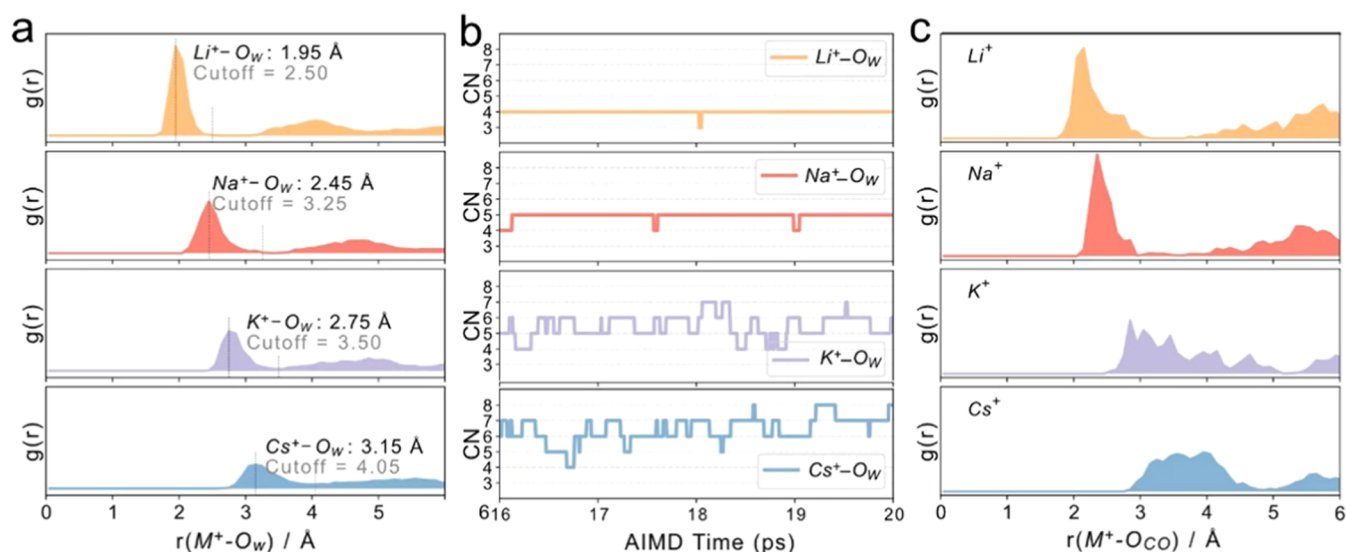


**Figure 6.** (a) Radial distribution functions (RDFs) of the cation and O atom in water ( $O_w$ ) in the Cu(100)/water system with different cations. (b) Evolution of  $M^+-O_w$  coordination numbers (CNs) in the Cu(100)/water system with different cations. The cutoff of the  $M^+-O_w$  bond was taken from the RDF in panel (a). (c) RDF of the cation and O atom in adsorbed CO in the system of  $\theta_{CO} = 6/25$  ML with different cations.

the charge extrapolation method,<sup>53</sup> the corrections for free energy barriers are less than 0.05 eV.

We further investigate the effect of the cation distribution on CO–CO coupling. We compare the  $\text{Na}^+$  ion at different positions under  $\theta_{CO} = 6/25$  ML, i.e., the  $\text{Na}^+$  ion in a fully solvated state at  $\sim 5.9$  Å above the Cu surface (outside the contact layer) and that in a partially dehydrated state closer to the Cu surface (within the contact layer). As shown in Figure 5a, the reaction free energy and active barrier for the latter case have distinctly decreased by 0.16 and 0.24 eV, compared with those of the former, which suggests that the migration of the  $\text{Na}^+$  ion toward the Cu slab should enhance the  $^*CO$  coupling in both thermodynamics and kinetics. The observed promotional role of cation migration is only based on the  $^*CO$  coupling step, regardless of the site-blocking effect from  $^*H$  adsorption. Previous work<sup>20</sup> has evidenced that the Faradaic current density of ethylene was declining as the electrode potential decreased from  $-0.6$  to  $-0.8$  V vs RHE, which can be ascribed to the site-blocking effect results from the competitive adsorption of H species as the potential negatively polarized.<sup>50</sup>

To further get insights into the  $^*CO$  coupling mechanism, we analyzed the Bader charges for the reactant  $^*CO$  along the reaction coordinate based on the trajectories from the constrained MD simulations. We found that in both cases the net charge of  $^*CO$  becomes more positive at first and then more negative during the  $^*CO$  coupling process (Figure 5b). The positive shift should result from the weakening of CO binding to the Cu surface at the initial stage of CO–CO coupling, which weakens the back-donation and makes C more positively charged (Figure S22a). When crossing the TS, the coupling process in fact corresponds to the reduction of the near-neutral CO species to an anionic form, with both C and O gaining electrons (Figure S22a–b), corresponding to the partial filling of  $\pi^*$  orbitals. At the TS, the CO is polarized the most, with the difference in charges on C and O reaching its maximum in the reaction profile,  $1.76|e|$  (Figure S22c). The presence of close-to-surface  $\text{Na}^+$  could interact with polar  $^*CO$  and lower the barrier of the charge transfer.

We further investigate the interplay between  $\text{Na}^+$  dynamics and  $^*CO$  coupling. Given the observed  $\text{Na}^+-OC^*$  inter-

mediate, we analyzed the distance between  $\text{Na}^+$  and O atoms in the reactant  $^*CO$  species (denoted as  $d_1$  and  $d_2$ , respectively) and the corresponding coordination numbers (CNs) along the reaction coordinates (i.e., C–C distances), as displayed in Figure 5c,d, respectively. At the early stage of CO–CO coupling ( $d_{C-C}$  ranges in 3.0–3.5 Å),  $d_1$  is significantly longer than  $d_2$  and the CN of the  $\text{Na}^+-O$  bond is 1, indicating that the  $\text{Na}^+$  ion only coordinates with one  $^*CO$ . As the two  $^*CO$  become closer ( $d_{C-C}$  ranges in 2.5–2.0 Å),  $\text{Na}^+$  drifts between the two terminal O atoms, with  $d_1$  slightly shorter than  $d_2$ . The total average CN is also slightly reduced, indicating a transition for the coordination of the  $\text{Na}^+$  ion with  $^*CO$ . When crossing the TS ( $d_{C-C}$  ranges 1.67–1.77 Å),  $d_1$  and  $d_2$  are sharply shortened, and the CN is near 2. This strong binding of the  $\text{Na}^+$  ion with pre-TS  $^*OCCO$  species greatly facilitates the charge transfer from the electrode to the  $^*OCCO$  intermediate and improves its stability. As the C–C bond formed,  $d_1$  and  $d_2$  gradually elongated ( $d_{C-C}$  ranges in 1.57–1.50 Å), and the CN decreased to 0, indicating that  $\text{Na}^+$  was released after the CO–CO coupling completed. Then, the released  $\text{Na}^+$  ion could again coordinate with the next  $^*CO$  species and initiate the next CO–CO coupling cycle. It should be noted that  $\text{Na}^+$  binding to the reactant  $^*CO$  is not tight but soft before the TS, as indicated by the larger fluctuations of  $d_1$  and  $d_2$  at CV = 2.0–3.0 Å, as shown in Figure S23. But after the TS, the binding of  $\text{Na}^+$  with  $O_{CO}$  becomes strong (especially at CV = 1.77 and 1.67 Å), which indicates that the main role of cations is to stabilize the strongly polar OCCO species after the TS and promote the electron transfer. Overall, the  $\text{Na}^+$  ion coordinates with  $^*CO$  in a dynamic manner along the reaction coordinate of  $^*CO$  coupling, significantly facilitating its thermodynamics and kinetics.

**3.4. Extension of the Dehydration Dynamics of Monovalent AM Cations.** Having understood the key role of cations' dehydration dynamics in the CO–CO coupling processes, we further discuss how the effect would differ for various AM cations. Since the cation–CO interaction relies on the dehydration of the first hydration shell, we expect cations with a more rigid hydration shell to have difficulty in dehydrating and penetrating into the contact layer<sup>54</sup> to access

the reaction intermediate. Smaller alkali metal cations would suffer from this issue the most, especially  $\text{Li}^+$ , which features a rigid first shell and a pronounced second shell.<sup>55</sup> Larger alkali metal and alkali earth cations, such as  $\text{Cs}^+$  and  $\text{Ba}^{2+}$ , would more easily dehydrate and make it closer to the catalyst surface.<sup>12</sup> Cation acidity is largely seen as an indicator of the cation–water solvent interaction,<sup>56</sup> which depends a lot on the size and valence of the ions. Specifically, the more acidic the cation is, the more difficult it is for the cation to get dehydrated due to the enhancing interaction with the water solvent, and vice versa. So, it can be estimated that the acidic cations such as  $\text{Mg}^{2+}$ ,  $\text{Nd}^{3+}$ , and  $\text{Al}^{3+}$ , compared with nonacidic cations, are less prone to dehydration and migration under specific CO coverage.

Without surprise, by analyzing the cation– $\text{O}_w$  ( $\text{O}_w$  refer to the O atom in water) radial distribution functions (RDFs) from AIMD trajectories (Figure 6a), we see that the compactness (cation–O distance of the first coordination shell) and hardness (width of the cation–O distance distribution and fluctuation of coordination numbers) (Figure 6b) of the hydration shells follow the trend of  $\text{Li}^+ > \text{Na}^+ > \text{K}^+ > \text{Cs}^+$ , which is in agreement with the findings by Monteiro et al.<sup>56</sup> This suggested that  $\text{Li}^+$  is the least prone to undergo dehydration and to promote CO–CO coupling, whereas  $\text{Cs}^+$  is the most. We also realize that the cation–CO interaction may also play a significant role in determining the activity order. In the AIMD of the Cu/water interface with CO coverage and cations, the cation–CO distance and interaction strength (estimated from cation–O RDF) have the trend of  $\text{Li}^+ > \text{Na}^+ > \text{K}^+ > \text{Cs}^+$  (from stronger to weaker interactions) (Figure 6c). Based on these results,  $\text{K}^+$  and  $\text{Cs}^+$  turn out to be the best cations that could not only effectively dehydrate to approach the activation complex but also dynamically release the  $\text{C}_2$  products due to their weak binding strength to the reaction intermediates. Our results are consistent with the extensive experimental reports that larger radius cations exhibit a better Faraday efficiency (or activity) toward  $\text{C}_2$  products.

We note that many of the key factors can be intercorrelating, with intrinsic connections among them. Hence, it is impossible to isolate and perform a single-variable analysis for each factor, and the relative strengths of them are unknown. In this work, we focus mainly on the cation vs no-cation comparison, and the analysis on comparing different cations is rather preliminary. A more detailed investigation into cationic effects is to follow. We believe that the hydration/dehydration dynamics, which we emphasize in this work, is a less straightforward but an important view angle to the cationic effects.

Whether the promotion effect can translate to other reactions is uncertain. CO–CO is unique in that it offers a highly polar TS (more polar than the IS and FS, Figure S22c) which can also serve as a bidentate ligand. As a result, the TS is the strongest interacting species with near-surface cations along the reaction profile. In addition, the CO–CO mechanism, which starts with CO–Cu weakening (which releases the back-donating electrons back to the surface Cu) and ends with the reduction of the  $^*\text{OCCO}$  complex, features a nonmonotonic charge transfer along the reaction coordinate (Figure 5b). Both of the geometric and electronic features underlie the reaction progress-dependent interfacial hydration/dehydration dynamics and migration of the cation. We expect a similar effect to be absent in reaction steps involving monoatomic species or monotonic electron transfer ( $\text{CO}_2$

activation,<sup>45</sup> HER/HOR, etc.), but likely to be present in reactions involving the dissociation/association of polyatomic intermediates (the dissociative pathway of the ORR<sup>46</sup> and the  $\text{N}_2\text{RR}$ <sup>57</sup>).

## 4. CONCLUSIONS

We have performed ab initio molecular dynamics (AIMD) simulations with the explicit water solvent to investigate CO–CO coupling over the Cu electrode under realistic  $\text{CO}_2\text{RR}$  conditions by employing AIMD simulations and free energy calculation. A variety of factors including CO coverage, water solvent, electrode potential, and alkali metal cations are taken into consideration. We have demonstrated the dehydration and migration of alkali metal cations induced by the increase of CO coverage in the electric double layer and found that the closer-to-surface dehydrated alkali metal cation can significantly promote CO–CO coupling. Specifically, the dehydrated alkali metal cation interacts with  $^*\text{CO}$  in a dynamic manner during the reaction, with adaptive binding distances and strengths, to modulate the reaction free energetics along the reaction coordinate. The geometric and electronic origins of such interfacial dynamics are analyzed in detail, with its implication to other cations and reactions discussed. This work provides a new perspective for understanding the dynamical aspect of the cationic effect on CO–CO coupling on the Cu surface, which could unlock a new dimension for optimizing the conditions to generate  $\text{C}_2$  products by modulating the surface coverage of CO. In addition, our study highlights the necessity of considering realistic aspects, such as explicit solvation and the electrochemical double layer, and the surface coverage of adsorbates. Combined with modeling electrocatalytic systems by AIMD simulations, the rich chemistry and dynamics at the electrode/electrolyte interface can be potentially captured.

## ■ ASSOCIATED CONTENT

### Supporting Information

The Supporting Information is available free of charge at <https://pubs.acs.org/doi/10.1021/acscatal.3c05812>.

Validation of the PBE functional, computational details for the model setup of the electrocatalytic interface, details for calculating the electrode potential and the coordination number, details for sampling the free energy profile via thermal integration, and input files and coordinates of the representative structural models (PDF)

## ■ AUTHOR INFORMATION

### Corresponding Author

Yang-Gang Wang – Department of Chemistry and Guangdong Provincial Key Laboratory of Catalysis, Southern University of Science and Technology, Shenzhen 518055 Guangdong, China; [orcid.org/0000-0002-0582-0855](https://orcid.org/0000-0002-0582-0855); Email: [wangyg@sustech.edu.cn](mailto:wangyg@sustech.edu.cn)

### Authors

Hui-Min Yan – Department of Chemistry and Guangdong Provincial Key Laboratory of Catalysis, Southern University of Science and Technology, Shenzhen 518055 Guangdong, China

Zisheng Zhang – Department of Chemistry and Biochemistry, University of California, Los Angeles, Los Angeles, California 90095, United States; [orcid.org/0000-0002-4370-4038](https://orcid.org/0000-0002-4370-4038)

Complete contact information is available at:  
<https://pubs.acs.org/10.1021/acscatal.3c05812>

## Notes

The authors declare no competing financial interest.

## ACKNOWLEDGMENTS

This work was financially supported by the NSFC (no. 22373045) of China, the Guangdong “Pearl River” Talent Plan (no. 2019QN01L353), the Science, Technology and Innovation Commission of Shenzhen Municipality (nos. KCXST20221021111207017 & JCYJ20220818100410023), and the Guangdong Provincial Key Laboratory of Catalysis (no. 2020B121201002). The computational resources were supported by the Center for Computational Science and Engineering at Southern University of Science and Technology (SUSTech) and the CHEM high-performance computing cluster (CHEM-HPC) at the Department of Chemistry, SUSTech.

## REFERENCES

- (1) Bushuyev, O. S.; De Luna, P.; Dinh, C. T.; Tao, L.; Saur, G.; van de Lagemaat, J.; Kelley, S. O.; Sargent, E. H. What should we make with CO<sub>2</sub> and how can we make it? *Joule* **2018**, *2*, 825–832.
- (2) Nitopi, S.; Bertheussen, E.; Scott, S. B.; Liu, X.; Engstfeld, A. K.; Horch, S.; Seger, B.; Stephens, I. E. L.; Chan, K.; Hahn, C.; Norskov, J. K.; Jaramillo, T. F.; Chorkendorff, I. Progress and perspectives of electrochemical CO<sub>2</sub> reduction on copper in aqueous electrolyte. *Chem. Rev.* **2019**, *119*, 7610–7672.
- (3) De Luna, P.; Hahn, C.; Higgins, D.; Jaffer, S. A.; Jaramillo, T. F.; Sargent, E. H. What would it take for renewably powered electrosynthesis to displace petrochemical processes? *Science* **2019**, *364*, No. eaav3506.
- (4) Chen, C.; Kotyk, J. F. K.; Sheehan, S. W. Progress toward commercial application of electrochemical carbon dioxide reduction. *Chem* **2018**, *4*, 2571–2586.
- (5) Gao, D.; Arán-Ais, R. M.; Jeon, H. S.; Cuenya, B. R. Rational catalyst and electrolyte design for CO<sub>2</sub> electroreduction towards multicarbon products. *Nat. Catal.* **2019**, *2*, 198–210.
- (6) Xie, H.; Wang, T.; Liang, J.; Li, Q.; Sun, S. Cu-based nanocatalysts for electrochemical reduction of CO<sub>2</sub>. *Nano Today* **2018**, *21*, 41–54.
- (7) Kuhl, K. P.; Cave, E. R.; Abram, D. N.; Jaramillo, T. F. New insights into the electrochemical reduction of carbon dioxide on metallic copper surfaces. *Energy Environ. Sci.* **2012**, *5*, 7050–7059.
- (8) Garza, A. J.; Bell, A. T.; Head-Gordon, M. Mechanism of CO<sub>2</sub> reduction at copper surfaces: pathways to C<sub>2</sub> products. *ACS Catal.* **2018**, *8*, 1490–1499.
- (9) Hori, Y.; Murata, A.; Takahashi, R. Formation of hydrocarbons in the electrochemical reduction of carbon dioxide at a copper electrode in aqueous solution. *J. Chem. Soc., Faraday Trans. 1* **1989**, *85*, 2309–2326.
- (10) Murata, A.; Hori, Y. Product selectivity affected by cationic species in electrochemical reduction of CO<sub>2</sub> and CO at a Cu electrode. *Bull. Chem. Soc. Jpn.* **1991**, *64*, 123–127.
- (11) Deng, B.; Huang, M.; Zhao, X.; Mou, S.; Dong, F. Interfacial electrolyte effects on electrocatalytic CO<sub>2</sub> reduction. *ACS Catal.* **2022**, *12*, 331–362.
- (12) Pérez-Gallent, E.; Marcandalli, G.; Figueiredo, M. C.; Calle-Vallejo, F.; Koper, M. T. M. Structure- and potential-dependent cation effects on CO reduction at copper single-crystal electrodes. *J. Am. Chem. Soc.* **2017**, *139*, 16412–16419.
- (13) Ringe, S.; Clark, E. L.; Resasco, J.; Walton, A.; Seger, B.; Bell, A. T.; Chan, K. Understanding cation effects in electrochemical CO<sub>2</sub> reduction. *Energy Environ. Sci.* **2019**, *12*, 3001–3014.
- (14) Pan, B.; Wang, Y.; Li, Y. Understanding and leveraging the effect of cations in the electrical double layer for electrochemical CO<sub>2</sub> reduction. *Chem. Catal.* **2022**, *2*, 1267–1276.
- (15) Kong, X.; Zhao, J.; Ke, J.; Wang, C.; Li, S.; Si, R.; Liu, B.; Zeng, J.; Geng, Z. Understanding the effect of \*CO coverage on C–C coupling toward CO<sub>2</sub> electroreduction. *Nano Lett.* **2022**, *22*, 3801–3808.
- (16) Hou, J.; Chang, X.; Li, J.; Xu, B.; Lu, Q. Correlating CO coverage and CO electroreduction on Cu via high-pressure in situ spectroscopic and reactivity investigations. *J. Am. Chem. Soc.* **2022**, *144*, 22202–22211.
- (17) Zhan, C.; Dattila, F.; Rettenmaier, C.; Bergmann, A.; Kuhl, S.; Garcia-Muelas, R.; Lopez, N.; Cuenya, B. R. Revealing the CO coverage-driven C–C coupling mechanism for electrochemical CO<sub>2</sub> reduction on Cu<sub>2</sub>O nanocubes via operando raman spectroscopy. *ACS Catal.* **2021**, *11*, 7694–7701.
- (18) Huang, Y.; Handoko, A. D.; Hirunsit, P.; Yeo, B. S. Electrochemical reduction of CO<sub>2</sub> using copper single-crystal surfaces: effects of CO\* coverage on the selective formation of ethylene. *ACS Catal.* **2017**, *7*, 1749–1756.
- (19) Li, J.; Wang, Z.; McCallum, C.; Xu, Y.; Li, F.; Wang, Y.; Gabardo, C. M.; Dinh, C.-T.; Zhuang, T.-T.; Wang, L.; Howe, J. Y.; Ren, Y.; Sargent, E. H.; Sinton, D. Constraining CO coverage on copper promotes high-efficiency ethylene electroproduction. *Nat. Catal.* **2019**, *2*, 1124–1131.
- (20) Schouten, K. J. P.; Gallent, E. P.; Koper, M. T. M. The influence of pH on the reduction of CO and CO<sub>2</sub> to hydrocarbons on copper electrodes. *J. Electroanal. Chem.* **2014**, *716*, 53–57.
- (21) Liu, X.; Schlexer, P.; Xiao, J.; Ji, Y.; Wang, L.; Sandberg, R. B.; Tang, M.; Brown, K. S.; Peng, H.; Ringe, S.; Hahn, C.; Jaramillo, T. F.; Norskov, J. K.; Chan, K. pH effects on the electrochemical reduction of CO<sub>2</sub> towards C<sub>2</sub> products on stepped copper. *Nat. Commun.* **2019**, *10*, No. 32.
- (22) Xiao, H.; Cheng, T.; Goddard, W. A., III; Sundararaman, R. Mechanistic explanation of the pH dependence and onset potentials for hydrocarbon products from electrochemical reduction of CO on Cu (111). *J. Am. Chem. Soc.* **2016**, *138*, 483–486.
- (23) Ma, W.; Xie, S.; Liu, T.; Fan, Q.; Ye, J.; Sun, F.; Jiang, Z.; Zhang, Q.; Cheng, J.; Wang, Y. Electrocatalytic reduction of CO<sub>2</sub> to ethylene and ethanol through hydrogen-assisted C–C coupling over fluorine-modified copper. *Nat. Catal.* **2020**, *3*, 478–487.
- (24) Goodpaster, J. D.; Bell, A. T.; Head-Gordon, M. Identification of possible pathways for C–C bond formation during electrochemical reduction of CO<sub>2</sub>: new theoretical insights from an improved electrochemical model. *J. Phys. Chem. Lett.* **2016**, *7*, 1471–1477.
- (25) Gauthier, J. A.; Lin, Z.; Head-Gordon, M.; Bell, A. T. Pathways for the formation of C<sub>2</sub><sup>+</sup> products under alkaline conditions during the electrochemical reduction of CO<sub>2</sub>. *ACS Energy Lett.* **2022**, *7*, 1679–1686.
- (26) Schouten, K. J. P.; Kwon, Y.; van der Ham, C. J. M.; Qin, Z.; Koper, M. T. M. A new mechanism for the selectivity to C<sub>1</sub> and C<sub>2</sub> species in the electrochemical reduction of carbon dioxide on copper electrodes. *Chem. Sci.* **2011**, *2*, 1902–1909.
- (27) Hori, Y.; Takahashi, R.; Yoshinami, Y.; Murata, A. Electrochemical reduction of CO at a copper electrode. *J. Phys. Chem. B* **1997**, *101*, 7075–7081.
- (28) Chang, X.; Li, J.; Xiong, H.; Zhang, H.; Xu, Y.; Xiao, H.; Lu, Q.; Xu, B. C–C Coupling Is Unlikely to Be the Rate-Determining Step in the Formation of C<sub>2</sub><sup>+</sup> Products in the Copper-Catalyzed Electrochemical Reduction of CO. *Angew. Chem., Int. Ed.* **2021**, *61*, No. e202111167.
- (29) Resasco, J.; Chen, L. D.; Clark, E.; Tsai, C.; Hahn, C.; Jaramillo, T. F.; Chan, K.; Bell, A. T. Promoter effects of alkali metal cations on the electrochemical reduction of carbon dioxide. *J. Am. Chem. Soc.* **2017**, *139*, 11277–11287.
- (30) Singh, M. R.; Kwon, Y.; Lum, Y.; Ager, J. W., III; Bell, A. T. Hydrolysis of electrolyte cations enhances the electrochemical reduction of CO<sub>2</sub> over Ag and Cu. *J. Am. Chem. Soc.* **2016**, *138*, 13006–13012.

- (31) Huang, B.; Rao, R. R.; You, S.; Hpone Myint, K.; Song, Y.; Wang, Y.; Ding, W.; Giordano, L.; Zhang, Y.; Wang, T.; Muy, S.; Katayama, Y.; Grossman, J. C.; Willard, A. P.; Xu, K.; Jiang, Y.; Shao-Horn, Y. Cation- and pH-dependent hydrogen evolution and oxidation reaction kinetics. *JACS Au* **2021**, *1*, 1674–1687.
- (32) Waegle, M. M.; Gunathunge, C. M.; Li, J.; Li, X. How cations affect the electric double layer and the rates and selectivity of electrocatalytic processes. *J. Chem. Phys.* **2019**, *151*, No. 160902.
- (33) Monteiro, M. C. O.; Dattila, F.; Hagedoorn, B.; García-Muelas, R.; López, N.; Koper, M. T. M. Absence of CO<sub>2</sub> electroreduction on copper, gold and silver electrodes without metal cations in solution. *Nat. Catal.* **2021**, *4*, 654–662.
- (34) Qin, X.; Vegge, T.; Hansen, H. A. Cation-coordinated inner-sphere CO<sub>2</sub> electroreduction at Au-water interfaces. *J. Am. Chem. Soc.* **2023**, *145*, 1897–1905.
- (35) Liu, H.; Liu, J.; Yang, B. Promotional role of a cation intermediate complex in C<sub>2</sub> formation from electrochemical reduction of CO<sub>2</sub> over Cu. *ACS Catal.* **2021**, *11*, 12336–12343.
- (36) Shin, S. J.; Choi, H.; Ringe, S.; Won, D. H.; Oh, H. S.; Kim, D. H.; Lee, T.; Nam, D. H.; Kim, H.; Choi, C. H. A unifying mechanism for cation effect modulating C<sub>1</sub> and C<sub>2</sub> productions from CO<sub>2</sub> electroreduction. *Nat. Commun.* **2022**, *13*, No. 5482.
- (37) Kresse, G.; Furthmüller, J. Efficient iterative schemes for ab initio total-energy calculations using a plane-wave basis set. *Phys. Rev. B* **1996**, *54*, 11169–11186.
- (38) Kresse, G.; Joubert, D. From ultrasoft pseudopotentials to the projector augmented-wave method. *Phys. Rev. B* **1999**, *59*, 1758–1775.
- (39) Blöchl, P. E. Projector augmented-wave method. *Phys. Rev. B* **1994**, *50*, 17953–17979.
- (40) Perdew, J. P.; Chevary, J. A.; Vosko, S. H.; Jackson, K. A.; Pederson, M. R.; Singh, D. J.; Fiolhais, C. Atoms, molecules, solids, and surfaces: Applications of the generalized gradient approximation for exchange and correlation. *Phys. Rev. B* **1992**, *46*, 6671–6687.
- (41) Perdew, J. P.; Burke, K.; Ernzerhof, M. Generalized gradient approximation made simple. *Phys. Rev. Lett.* **1996**, *77*, 3865–3868.
- (42) Grimme, S.; Antony, J.; Ehrlich, S.; Krieg, H. A consistent and accurate ab initio parametrization of density functional dispersion correction (DFT-D) for the 94 elements H-Pu. *J. Chem. Phys.* **2010**, *132*, No. 154104.
- (43) Nosé, S. A unified formulation of the constant temperature molecular dynamics methods. *J. Chem. Phys.* **1984**, *81*, 511–519.
- (44) Hoover, W. G. Canonical dynamics: Equilibrium phase-space distributions. *Phys. Rev. A* **1985**, *31*, 1695–1697.
- (45) Cao, H.; Zhang, Z.; Chen, J.-W.; Wang, Y.-G. Potential-dependent free energy relationship in interpreting the electrochemical performance of CO<sub>2</sub> reduction on single atom catalysts. *ACS Catal.* **2022**, *12*, 6606–6617.
- (46) Chen, J. W.; Zhang, Z.; Yan, H. M.; Xia, G. J.; Cao, H.; Wang, Y. G. Pseudo-adsorption and long-range redox coupling during oxygen reduction reaction on single atom electrocatalyst. *Nat. Commun.* **2022**, *13*, No. 1734.
- (47) Carter, E. A.; Ciccotti, G.; Hynes, J. T.; Kapral, R. Constrained reaction coordinate dynamics for the simulation of rare events. *Chem. Phys. Lett.* **1989**, *156*, 472–477.
- (48) Humphrey, W.; Dalke, A.; Schulten, K. VMD: Visual Molecular Dynamics. *J. Mol. Graphics* **1996**, *14*, 33–38.
- (49) Baricuatro, J. H.; Kim, Y.-G.; Korzeniewski, C. L.; Soriaga, M. P. Seriatim ECSTM-ECPMIRS of the adsorption of carbon monoxide on Cu(100) in alkaline solution at CO<sub>2</sub>-reduction potentials. *Electrochem. Commun.* **2018**, *91*, 1–4.
- (50) Hollins, P.; Pritchard, J. Interactions of CO molecules adsorbed on Cu(111). *Surf. Sci.* **1979**, *89*, 486–495.
- (51) Harendt, C.; Goschnick, J.; Hirschwald, W. The interaction of CO with copper (110) studied by TDS and LEED. *Surf. Sci.* **1985**, *152–153*, 453–462.
- (52) Tracy, J. C. Structural Influences on Adsorption Energy. III. CO on Cu(100). *J. Chem. Phys.* **1972**, *56*, 2748–2754.
- (53) Chan, K.; Norskov, J. K. Electrochemical barriers made simple. *J. Phys. Chem. Lett.* **2015**, *6*, 2663–2668.
- (54) Shah, A. H.; Zhang, Z.; Huang, Y.; Wang, S.; Zhong, G.; Wan, C.; Alexandrova, A. N.; Huang, Y.; Duan, X. The role of alkali metal cations and platinum-surface hydroxyl in the alkaline hydrogen evolution reaction. *Nat. Catal.* **2022**, *5*, 923–933.
- (55) Kiyohara, K.; Minami, R. Hydration and dehydration of monovalent cations near an electrode surface. *J. Chem. Phys.* **2018**, *149*, No. 014705.
- (56) Monteiro, M. C. O.; Dattila, F.; López, N.; Koper, M. T. M. The role of cation acidity on the competition between hydrogen evolution and CO<sub>2</sub> reduction on gold electrodes. *J. Am. Chem. Soc.* **2022**, *144*, 1589–1602.
- (57) Qian, S.-J.; Cao, H.; Chen, J.-W.; Chen, J.-C.; Wang, Y.-G.; Li, J. Critical role of explicit inclusion of solvent and electrode potential in the electrochemical description of nitrogen reduction. *ACS Catal.* **2022**, *12*, 11530–11540.